Contamination of the Bushveld Complex (South Africa) magmas by basinal brines: Stable isotopes in phlogopite from the UG2 chromitite

Haoyang Zhou[1,2]*, Robert B. Trumbull[1], Ilya V. Veksler[1,3], Ilya N. Bindeman[4], Johannes Glodny[1], Felix E.D. Kaufmann[5], and Dieter Rammlmair[6]

[1]*GFZ German Research Centre for Geosciences, Telegrafenberg, Potsdam 14473, Germany*

[2]*Natural History Museum, University of Oslo, Blindern, Oslo 0318, Norway*

[3]*Institute of Geosciences, University of Potsdam, Potsdam-Golm 14476, Germany*

[4]*Department of Earth Sciences, University of Oregon, Eugene, Oregon 97403-1272, USA*

[5]*Museum für Naturkunde Berlin, Invalidenstrasse 43, Berlin 10115, Germany*

[6]*Federal Institute for Geosciences and Natural Resources (BGR), Hannover 30655, Germany*

* Email: haoyang.zhou@nhm.uio.no, ORCID: 0000-0002-0079-503X

SAMPLE INFORMATION

We investigated phlogopite in the Upper Group 2 (UG2) chromitite and adjacent silicate wall rocks in 1.4-m drill-core sections from each of the Nkwe and Khuseleka mine sites in the eastern and western limbs of the Bushveld Complex (South Africa), respectively. Details of the deposit geology and mineral-chemical features of these two mines can be found in Veksler et al. (2018). In addition, we analyzed phlogopite samples in UG2 chromitite from two 1.6-m drill-core sections (4048 and 4049) taken from the Karee mine in the western limb. Descriptions of the deposit

geology and mineral-chemical features of the UG2 section can be found in Junge et al. (2014).

METHODOLOGY

Mineral distribution mapping

Qualitative element distribution mapping was done by micro-X-ray fluorescence (micro-XRF) analysis of thin sections using a Bruker M4-Tornado at the Federal Institute for Geosciences and Natural Resources (BGR), Hannover. The instrument used a Rh tube at 50 kV and 600 µA, with a polycapillary beam of 17-µm spot size (at Mo Kα). The step size was 20 µm and acquisition time at each point was 4 ms. To minimize phase diffraction signals interfering with the element spectra of interest (Nikonow and Rammlmair, 2016), we used two opposing solid-state detectors with take-off angles of 51° and 90° to the X-ray tube (whose incident angle is 51° from the sample surface). This provided spectral data cubes from which the minimum signal per channel and pixel of both detectors was extracted for selected element spectra of interest to create element distribution maps free of diffraction effects. Phase analysis from the element distribution was done with the ENVI-IDL-based BGR software Petrographic Analyst (Nikonow and Rammlmair, 2017), which is based on spectral libraries of endmembers for the minerals of interest derived from independent standards and/or known mineral grains on the samples themselves. The method is analogous to the familiar electron-beam methods of phase mapping QEMSCAN or mineral liberation analyzer (MLA). Examples of phase distribution maps and maps of phlogopite distribution alone are given in Fig. S1 and the qualitative modal abundance of phlogopite in each locality is listed in Table S1.

Electron microprobe analysis

The composition of phlogopite was measured on polished thin sections at the Museum für Naturkunde Berlin using a JEOL JXA-8500F electron probe microanalyzer (EPMA) with a field

emission cathode and five wave-length-dispersive spectrometers. Operating conditions were an accelerating voltage of 15 kV, a beam current of 15 nA, and a probe diameter of 5 μm. The analyzed elements and corresponding standards, peak and background counting time, and average detection limits are as follow: SiO_2 (Cr-augite, 20 s and 10 s, 0.022 wt%), TiO_2 (ilmenite, 40 s and 20 s, 0.016 wt%), Al_2O_3 (osumilite, 20 s and 10 s, 0.016 wt%), Cr_2O_3 (Cr-augite, 20 s and 10 s, 0.026 wt%), V_2O_3 (native vanadium, 40 s and 20 s, 0.013 wt%), FeO (ilmenite, 20 s and 10 s, 0.021 wt%), MgO (Cr-augite, 20 s and 10 s, 0.015 wt%), MnO (ilmenite, 20 s and 10 s, 0.021 wt%), CaO (Cr-augite, 20 s and 10 s, 0.008 wt%), Na_2O (anorthoclase, 10 s and 5 s, 0.018 wt%), K_2O (osumilite, 10 s and 5 s, 0.008 wt%), F [apatite-(CaF), 80 s and 40 s, 0.073 wt%], and Cl (tugtupite, 40 s and 20 s, 0.003 wt%). Natural minerals of the Smithsonian international standard suite (Jarosewich et al. 1980) and minerals and metals of the Astimex standard were used to calibrate the measured intensities. All analyses were processed by a ZAF routine by the JEOL series operating system to minimize matrix effects. Data are given in Table S1.

Separation of phlogopite

Phlogopite mineral separates were prepared using ~10 g of rock fragments per sample. Samples were crushed by hammering on a steel plate and then sieved. Only fragments with grain sizes > 63 μm were collected for separation. Phlogopite was pre-concentrated manually using clear paper as a "dry shaking table" that tends to retain tabular phlogopite and shakes off most heavy and equant minerals. After pre-concentration, magnetic sorting was applied using a Frantz magnetic separator to further remove chromite (high magnetic susceptibility) and plagioclase (low magnetic susceptibility). The phlogopite-concentrated fractions were then carefully ground in a polished agate mortar filled with ethanol. Due to its elasticity in thin layers, combined with toughness and perfect basal cleavage, phlogopite resists comminution by grinding compared to other typically brittle minerals (chromite, plagioclase, and orthopyroxene) and retains a larger

grain size. Therefore, fairly pure separates of phlogopite were recovered by sieving and retaining grains > 63 µm. The purity of the final mineral fraction was enhanced by picking under a binocular microscope. Around 2–20-mg phlogopite was finally obtained for each sample.

Hydrogen and triple-oxygen isotope analysis

The hydrogen and triple-oxygen isotopic ratios were measured on a MAT253 mass spectrometer at the University of Oregon Stable Isotope Lab. The mass spectrometer is equipped with a laser fluorination line (used for oxygen isotope analysis) and is connected to a high-temperature thermal conversion elemental analyzer (TC/EA; used for hydrogen isotope and H_2O content analyses). H_2O contents and hydrogen isotopes were measured following the analytical protocol described in Martin et al. (2017). Around 1-mg phlogopite was heated to react with vitreous carbon to produce H_2 (and CO). Hydrogen isotopic ratios were analyzed by the TC/EA-MAT253 using a continuous flow model, while water contents were calculated via peak integration.

Oxygen isotopes were measured following the analytical protocol described in Bindeman et al. (2014). Around 1.2-mg phlogopite was loaded and reacted with BrF_5 to release O_2. The oxygen gas was converted to CO_2 by a platinum-graphite converter, and $^{18}O/^{16}O$ ratios were analyzed by the MAT253 mass spectrometer. Triple-oxygen isotopic compositions were measured following the analytical protocol described in Zakharov et al. (2017). Around 1.2–1.4-mg phlogopite was used to extract O_2 by CO_2-laser fluorination. The oxygen gas was purified using a gas chromatographic column and ratios of $^{18}O/^{16}O$ and $^{17}O/^{16}O$ were measured in the MAT253 mass spectrometer.

The δD, $δ^{18}O$, and $Δ'^{17}O$ values are reported relative to the Vienna Standard Mean Ocean Water (VSMOW) scale. $Δ'^{17}O$ is the deviation of a linearized $δ^{17}O$ ($δ'^{17}O$) from the values defined by a reference line with a slope (λ) of 0.5305 and is calculated as $Δ'^{17}O = δ'^{17}O – 0.5305 × δ'^{18}O$, where $δ'^{17,18}O = 1000 × \ln(δ^{17,18}O/1000 + 1)$. The average internal precisions within 1 standard

deviation are ± 1–4‰ for δD, better than ± 0.1‰ for $\delta^{18}O$, and ± 0.01‰ for $\Delta'^{17}O$.

Mass balance modeling

Here we give details of estimating δD, $\delta^{18}O$, and $\Delta'^{17}O$ (λ = 0.5305) values for the three endmembers (mantle-derived magma, crustal contaminant, and external fluids) used in computing the isotope mixing lines shown in Fig. 4B and Fig. S7.

The mantle-derived magma was assigned a δD of −75‰ (Loewen et al., 2019), $\delta^{18}O$ of 5.7‰ (Ito et al., 1987), and $\Delta'^{17}O$ of −0.052‰ (Miller et al., 2020). The concentration of O in the magma is taken as 50 wt%, while H_2O content is set at 0.3 wt% based on loss of ignition (LOI) results of chemical analyses of B1-type sills (parental melt for the CZ) by Barnes et al. (2010).

Possible crustal contaminants for the Rustenburg Layered Suite (RLS) magmas include: (1) Transvaal Supergroup marine-deltaic sediments (sandstones and shales), and (2) Archean basement rocks in the lower to mid-crust (Harris et al., 2005). Considering first the Transvaal sediment contaminant, Harris et al. (2005) argued that 20% contamination of mantle-derived magmas would explain the magmatic $\delta^{18}O$ composition for RLS, although they doubted the feasibility of having such an amount of material in the deep crust. Bindeman et al. (2018) measured triple-oxygen isotope ratios in the range of −0.149‰ to −0.103‰ ($\delta^{18}O$ = 9.6‰ to 11.2‰; n=12) for the shales in the Timeball Hill Formation of the lower Pretoria Group (the floor of the Bushveld Complex) from the upper Transvaal Supergroup. Taking the same amount of contamination from Harris et al. (2005) and the $\Delta'^{17}O$ values from Bindeman et al. (2018), our calculation shows that it would produce magmatic $\Delta'^{17}O$ maximizing at −0.063‰, which is lower than all but one of the UG2 values. Therefore, we do not consider the Transvaal sediments as the dominant contaminant.

Following Harris et al. (2005), the lower to mid-crustal contaminant is assumed to be Archean crystalline rocks such as granitic gneiss exposed in the nearby Vredefort Dome, or the amphibolite to granulite-facies metapelites in the Limpopo Belt to the north of Bushveld. Those lithologies

have mean $\delta^{18}O$ values of 9.2‰ and 9.6‰, respectively (Harris et al., 2005) and we used 9.4‰ for the $\delta^{18}O$ value of the deep crustal contaminant. Its $\Delta'^{17}O$ value is calculated to be −0.067‰ based on the relation $\delta'^{17}O = \lambda_{RL} \times \delta'^{18}O$ and world average "crustal array" λ_{RL} of 0.5233 as argued in Bindeman (2021). Given the low hydrogen content of the potential crustal contaminants, we assume that lower or mid-crustal contamination had negligible impact on the magmatic D/H ratio of the RLS magmas, and this is supported by the fact that bulk-rock δD values of the RLS (−99‰ to −53‰) center around the mantle value of -75‰ (Loewen et al., 2019). The O concentration is assumed to be 50 wt% for the lower to mid-crustal contaminant, the same as for the Bushveld magma.

The external fluids were assumed to be connate water (seawater) in the marine deltaic sandstone-shale sequences of the Pretoria Group, which underlie the Bushveld eastern and western limbs and must have released water by contact metamorphism during emplacement of Bushveld magmas (Benson et al., 2020 and references therein). Estimations of Precambrian seawater composition (Pope et al., 2012; Zakharov and Bindeman, 2019) suggest similar O-isotope compositions as today but an evolution in δD values from −25‰ ± 5‰ at 3.8 Ga to 0‰ ± 20‰ at the age of Pretoria Group deposition at ca. 2.2–2.1 Ga. Moreover, Schiffries and Rye (1990) reported δD values of −34‰ for fluid inclusions in quartzite from the contact aureole of the Bushveld Complex. We assumed a range from −30‰ to 0‰ as the δD values for Transvaal brines. The values for $\delta^{18}O$ and $\Delta'^{17}O$ were set at 5‰ and −0.025‰, respectively, as suggested for pore fluids by Bindeman (2021). For calculation, we assume the fluids have stoichiometric H and O concentrations of pure H_2O.

The deep-crustal contamination (step 1 on Fig. 4B and Fig. S7) involved mixing of the lower to mid-crustal components with mantle-derived magmas. The mixing computation shows that the

$\Delta'^{17}O$ composition of the UG2 melts can be explained by as much as 30%–40% crustal contaminant. Specifically, 30% of crustal contaminant would yield a magmatic $\delta^{18}O$ of 6.8‰ (equivalent $\Delta'^{17}O = -0.057‰$), which agrees with the average $\delta^{18}O$ of the Critical Zone given by Schiffries and Rye (1989), whereas 40% is needed to match the average $\delta^{18}O$ of 7.2‰ (equivalent $\Delta'^{17}O$ of $-0.059‰$) given by Harris et al. (2005) for the entire RLS. The step 2 model uses these values from step 1 as the starting compositions to calculate mixing curves with connate seawater in the Pretoria Group sediments.

REFERENCES CITED

Benson, E., Connolly, J.A. and Boudreau, A.E., 2020, Crustal fluid contamination in the Bushveld Complex, South Africa: An analogue for subduction zone fluid migration: International Geology Review, doi: 10.1080/00206814.2020.1795734.

Bindeman, I.N., Serebryakov, N.S., Schmitt, A.K., Vazquez, J.A., Guan, Y., Azimov, P.Y., Astafiev, B.Y., Palandri, J., and Dobrzhinetskaya, L., 2014, Field and microanalytical isotopic investigation of ultradepleted in ^{18}O Paleoproterozoic "Slushball Earth" rocks from Karelia, Russia: Geosphere, v. 10, p. 308–339.

Bindeman, I.N., Zakharov, D.O., Palandri, J., Greber, N.D., Dauphas, N., Retallack, G.J., Hofmann, A., Lackey, J.S., and Bekker, A., 2018, Rapid emergence of subaerial landmasses and onset of a modern hydrologic cycle 2.5 billion years ago: Nature, v. 557, p. 545–548.

Bindeman, I.N., 2021, Triple oxygen isotopes in evolving continental crust, granites, and clastic sediments: Reviews in Mineralogy and Geochemistry, v. 86, p. 241–290.

Harris, C., and Chaumba, J.B., 2001, Crustal contamination and fluid–rock interaction during the formation of the Platreef, northern limb of the Bushveld Complex, South Africa: Journal of Petrology, v. 42, p. 1321–1347.

Harris, C., Pronost, J.J.M., Ashwal, L.D., and Cawthorn, R.G., 2005, Oxygen and hydrogen
    isotope stratigraphy of the Rustenburg Layered Suite, Bushveld Complex: Constraints on
    crustal contamination: Journal of Petrology, v. 46, p. 579–601.

Ito, E., White, W.M., and Göpel, C., 1987, The O, Sr, Nd and Pb isotope geochemistry of MORB:
    Chemical Geology, v. 62, p. 157–176.

Jarosewich, E., Nelen, J. A., and Norberg, J. A., 1980, Reference samples for electron microprobe
    analysis. Geostandards Newsletter, v. 4, p. 43–47.

Junge, M., Oberthür, T., and Melcher, F., 2014, Cryptic variation of chromite chemistry, platinum
    group element and platinum group mineral distribution in the UG-2 chromitite: an example
    from the Karee Mine, western Bushveld Complex, South Africa: Economic Geology, v. 109,
    p. 795–810.

Loewen, M.W., Graham, D.W., Bindeman, I.N., Lupton, J.E., and Garcia, M.O., 2019, Hydrogen
    isotopes in high ^{3}He/^{4}He submarine basalts: Primordial vs. recycled water and the veil of
    mantle enrichment: Earth and planetary science letters, v. 508, p. 62–73.

Martin, E., Bindeman, I., Balan, E., Palandri, J., Seligman, A., and Villemant, B., 2017, Hydrogen
    isotope determination by TC/EA technique in application to volcanic glass as a window into
    secondary hydration: Journal of Volcanology and Geothermal Research, v. 348, p. 49–61.

Miller, M.F., Pack, A., Bindeman, I.N., and Greenwood, R.C., 2020, Standardizing the reporting
    of Δ'^{17}O data from high precision oxygen triple-isotope ratio measurements of silicate rocks
    and minerals: Chemical Geology, v. 532, p. 119332.

Nikonow, W., and Rammlmair, D., 2017, Automated mineralogy based on micro-energy-
    dispersive X-ray fluorescence microscopy (μ-EDXRF) applied to plutonic rock thin sections
    in comparison to a mineral liberation analyzer: Geoscientific Instrumentation, Methods and

Data Systems, v. 6, p. 429–437.

Nikonow, W., and Rammlmair, D., 2016, Risk and benefit of diffraction in Energy Dispersive X-ray fluorescence mapping: Spectrochimica Acta Part B: Atomic Spectroscopy, v. 125, p. 120–126.

Pope, E.C., Bird, D.K. and Rosing, M.T., 2012, Isotope composition and volume of Earth's early oceans: Proceedings of the National Academy of Sciences, v. 109, p. 4371–4376.

Schiffries, C.M., and Rye, D.M., 1989, Stable isotopic systematics of the Bushveld Complex; I, Constraints of magmatic processes in layered intrusions: American Journal of Science, v. 289, p. 841–873.

Schiffries, C.M., and Rye, D.M., 1990, Stable isotopic systematics of the Bushveld Complex; II, Constraints on hydrothermal processes in layered intrusions: American Journal of Science, v. 290, p. 209–245.

Veksler, I.V., Sedunova, A.P., Darin, A.V., Anosova, M.O., Reid, D.L., Kaufmann, F.E.D., Hecht, L., and Trumbull, R.B., 2018, Chemical and textural re-equilibration in the UG2 chromitite layer of the Bushveld Complex, South Africa: Journal of Petrology, v. 59, p. 1193–1216.

Zakharov, D.O., and Bindeman, I.N., 2019, Triple oxygen and hydrogen isotopic study of hydrothermally altered rocks from the 2.43–2.41 Ga Vetreny belt, Russia: An insight into the early Paleoproterozoic seawater: Geochimica et Cosmochimica Acta, v. 248, p. 185–209.

Zakharov, D.O., Bindeman, I.N., Slabunov, A.I., Ovtcharova, M., Coble, M.A., Serebryakov, N.S., and Schaltegger, U., 2017, Dating the Paleoproterozoic snowball Earth glaciations using contemporaneous subglacial hydrothermal systems: Geology, v. 45, p. 667–670.
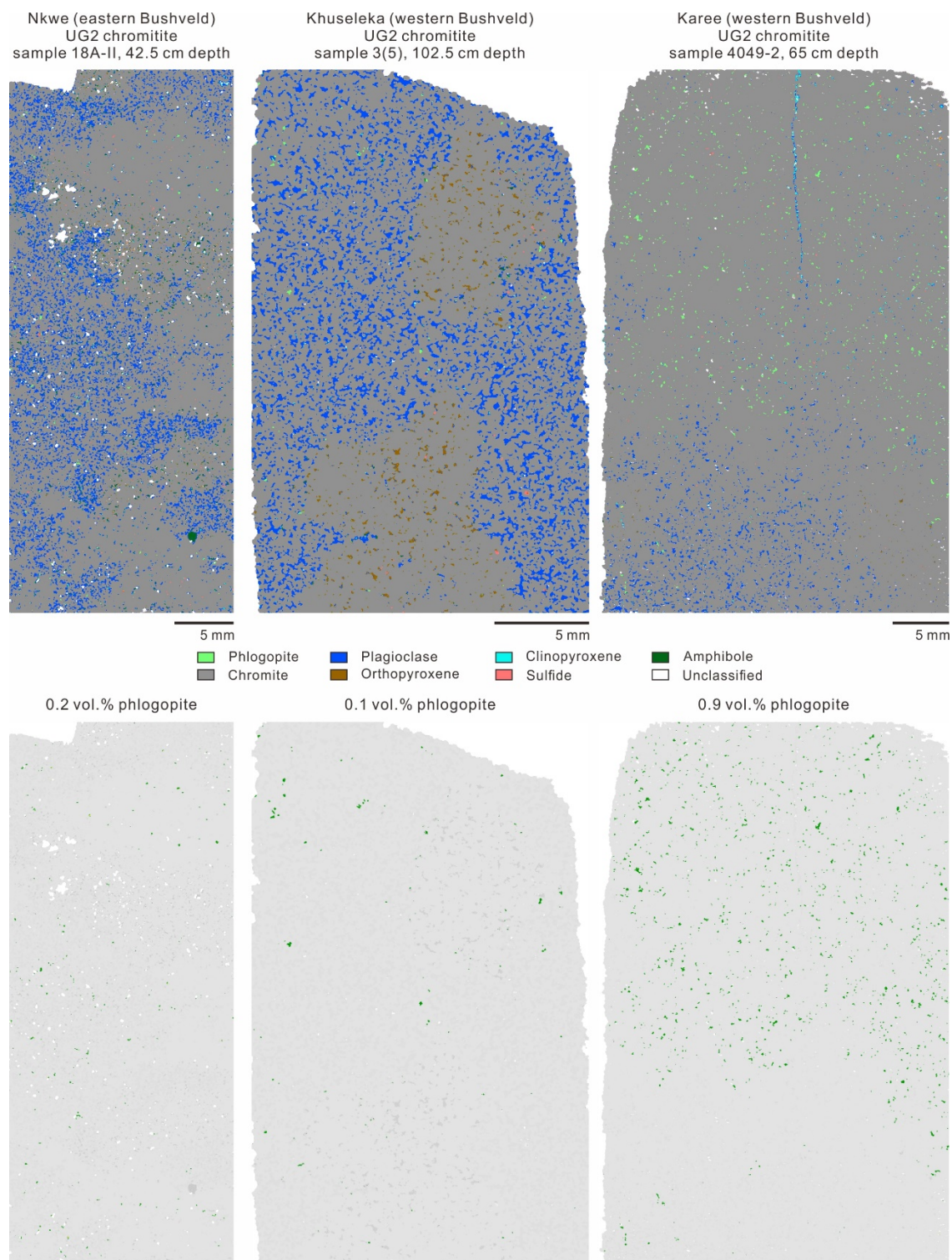
Figure S1. Representative maps of phase distribution and of phlogopite distribution alone in the UG2 chromitite (Bushveld Complex, South Africa) from the Nkwe, Khuseleka, and Karee mines.
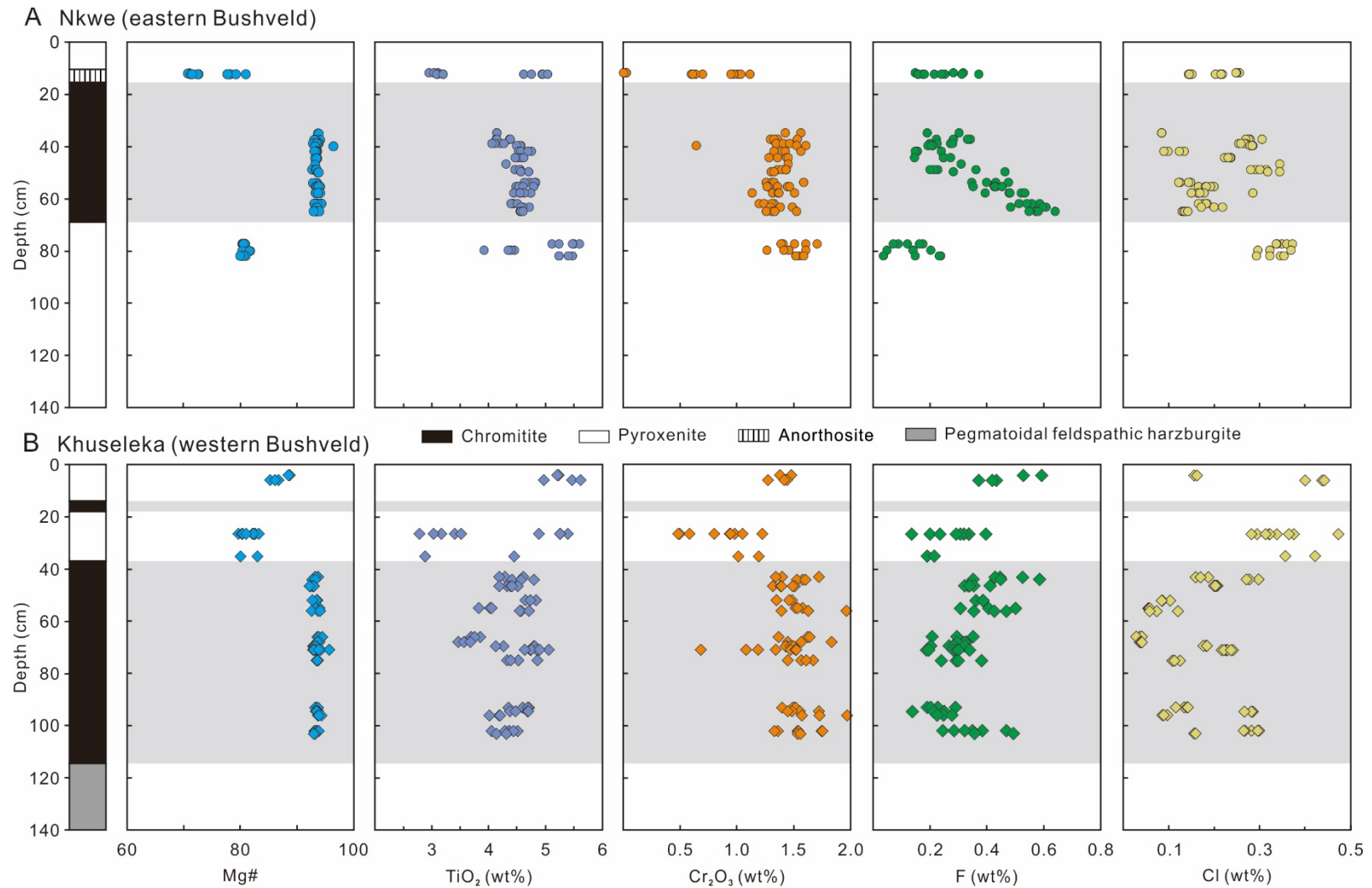
Figure S2. Variations in Mg# [$100 \times Mg/(Mg + Fe^{2+})$], TiO_2, Cr_2O_3, F, and Cl contents of phlogopite from the UG2 chromitite and adjacent silicate cumulates (Bushveld Complex, South Africa) in the Nkwe and Khuseleka mines.
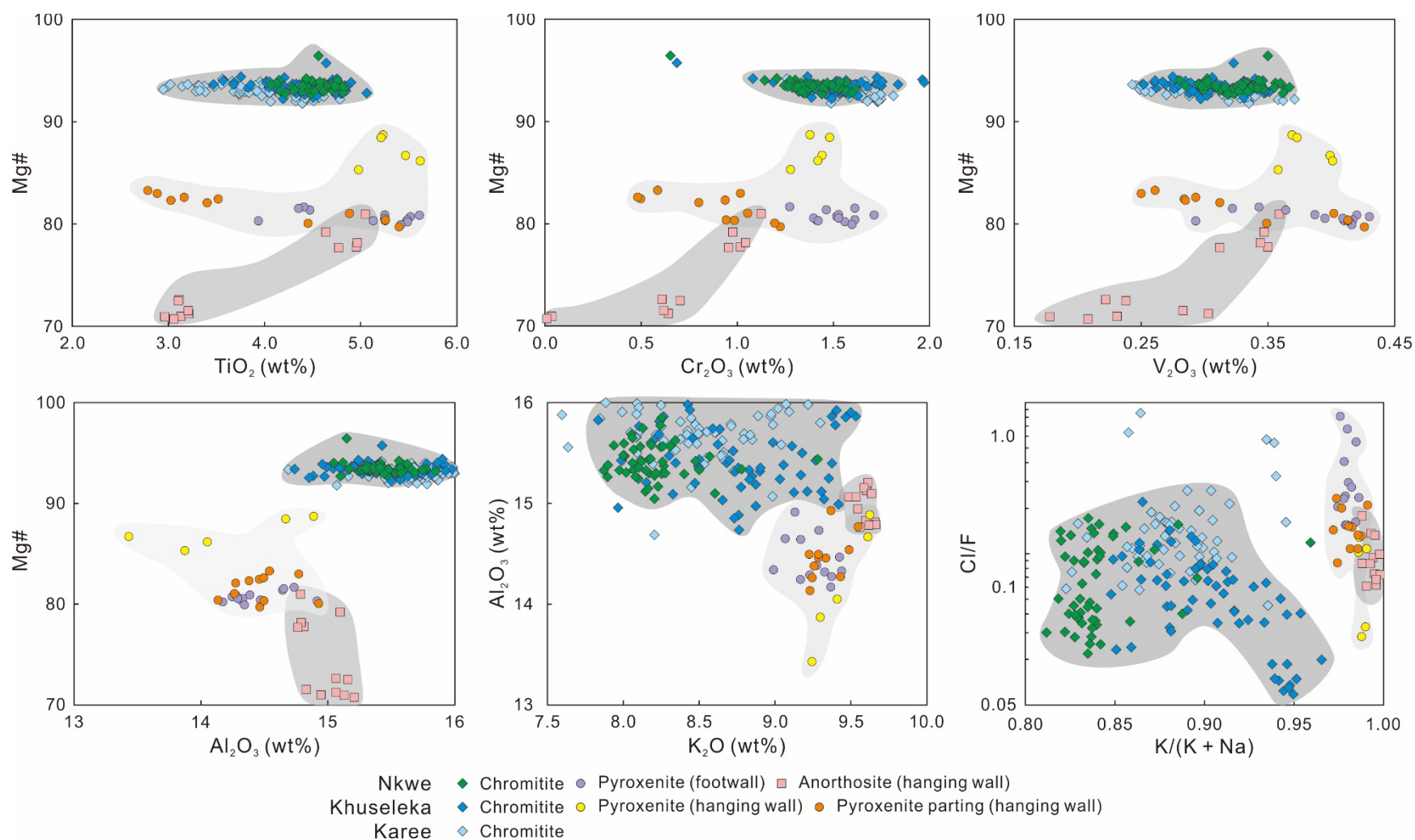
Figure S3. Relationships between Mg# [$100 \times Mg/(Mg + Fe^{2+})$], contents of Ti₂O, Cr₂O₃, V₂O₃, Al₂O₃, K₂O, and molar ratios of Cl/F and K/(K + Na) of phlogopite from the UG2 chromitite and adjacent silicate cumulates (Bushveld Complex, South Africa) in the Nkwe, Khuseleka, and Karee mines.

Figure S4. Relationships between H_2O content and δD, $\delta^{18}O$ values for phlogopite from the UG2 chromitite and adjacent silicate cumulates (Bushveld Complex, South Africa) in the Nkwe, Khuseleka, and Karee mines.
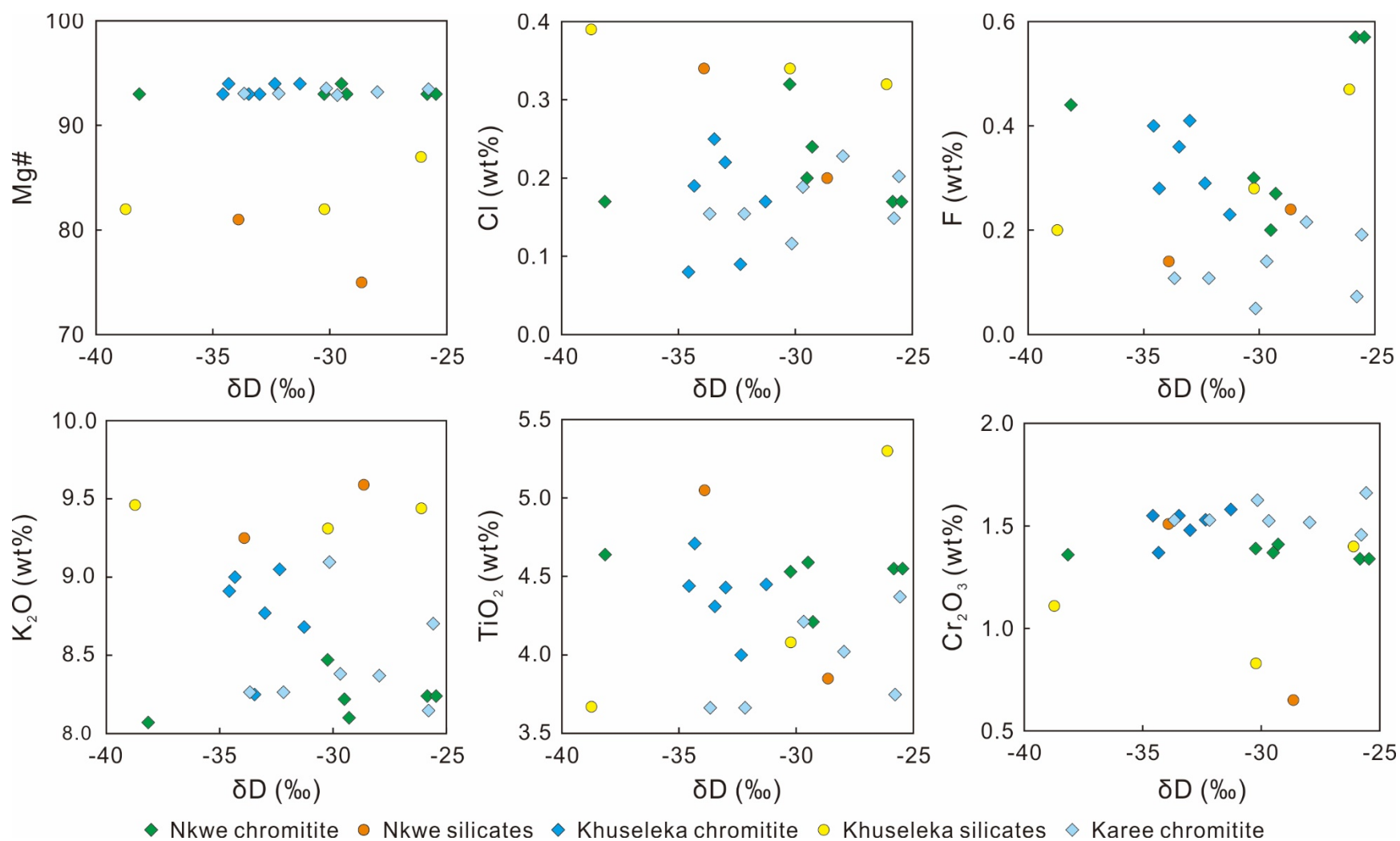
Figure S5. Relationships between δD value and Mg# [100 × Mg/(Mg + Fe^{2+})], Cl, F, K$_2$O, Ti$_2$O, and Cr$_2$O$_3$ contents of phlogopite from the UG2 chromitite and adjacent silicate cumulates (Bushveld Complex, South Africa) in the Nkwe, Khuseleka, and Karee mines.
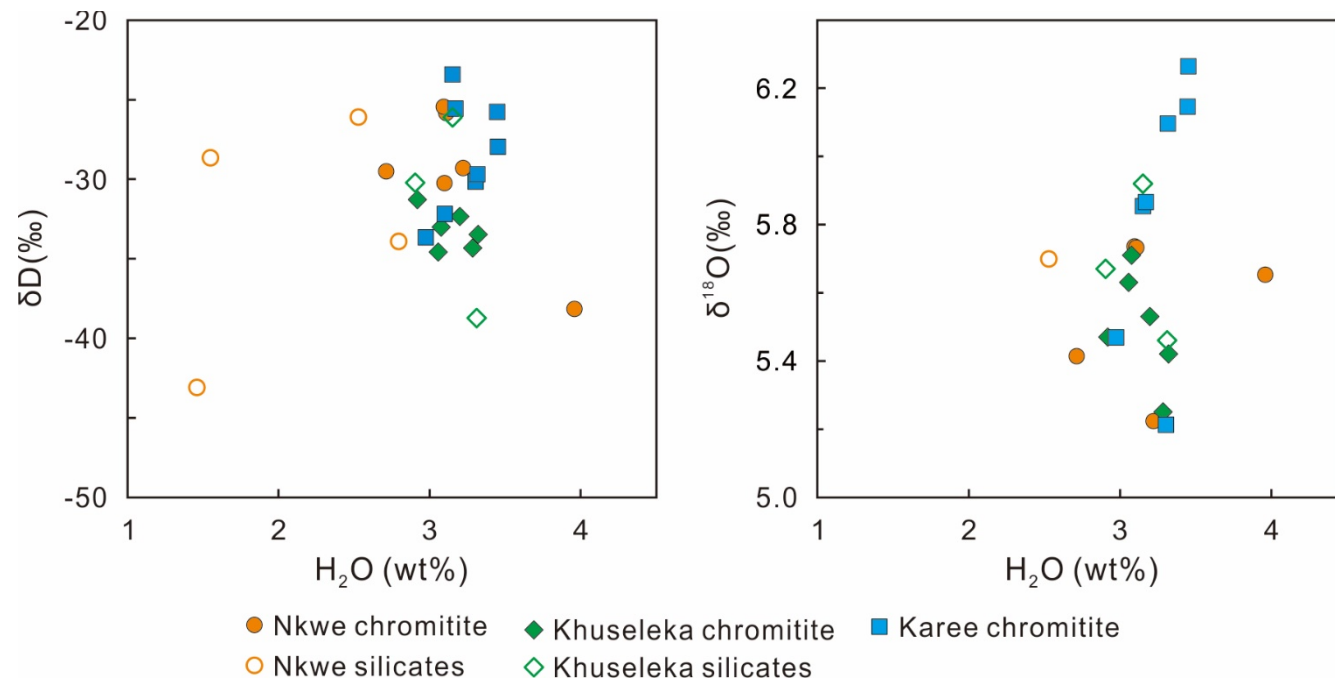
Figure S6. Relationships between $\delta^{18}O$ value and Mg# [$100 \times Mg/(Mg + Fe^{2+})$], Cl, F, K_2O, Ti_2O, and Cr_2O_3 contents of phlogopite from the UG2 chromitite and adjacent silicate cumulates (Bushveld Complex, South Africa) in the Nkwe, Khuseleka, and Karee mines.
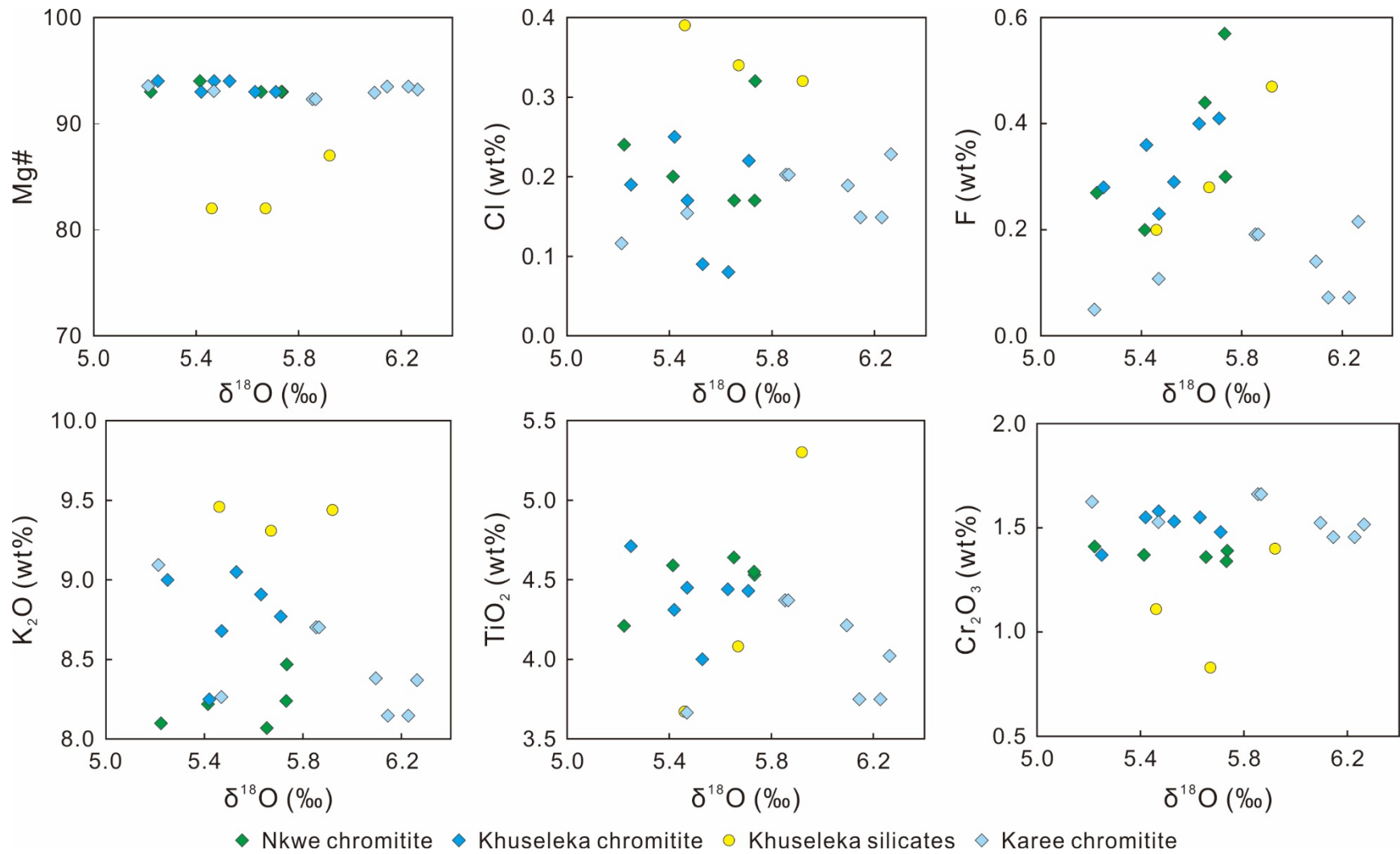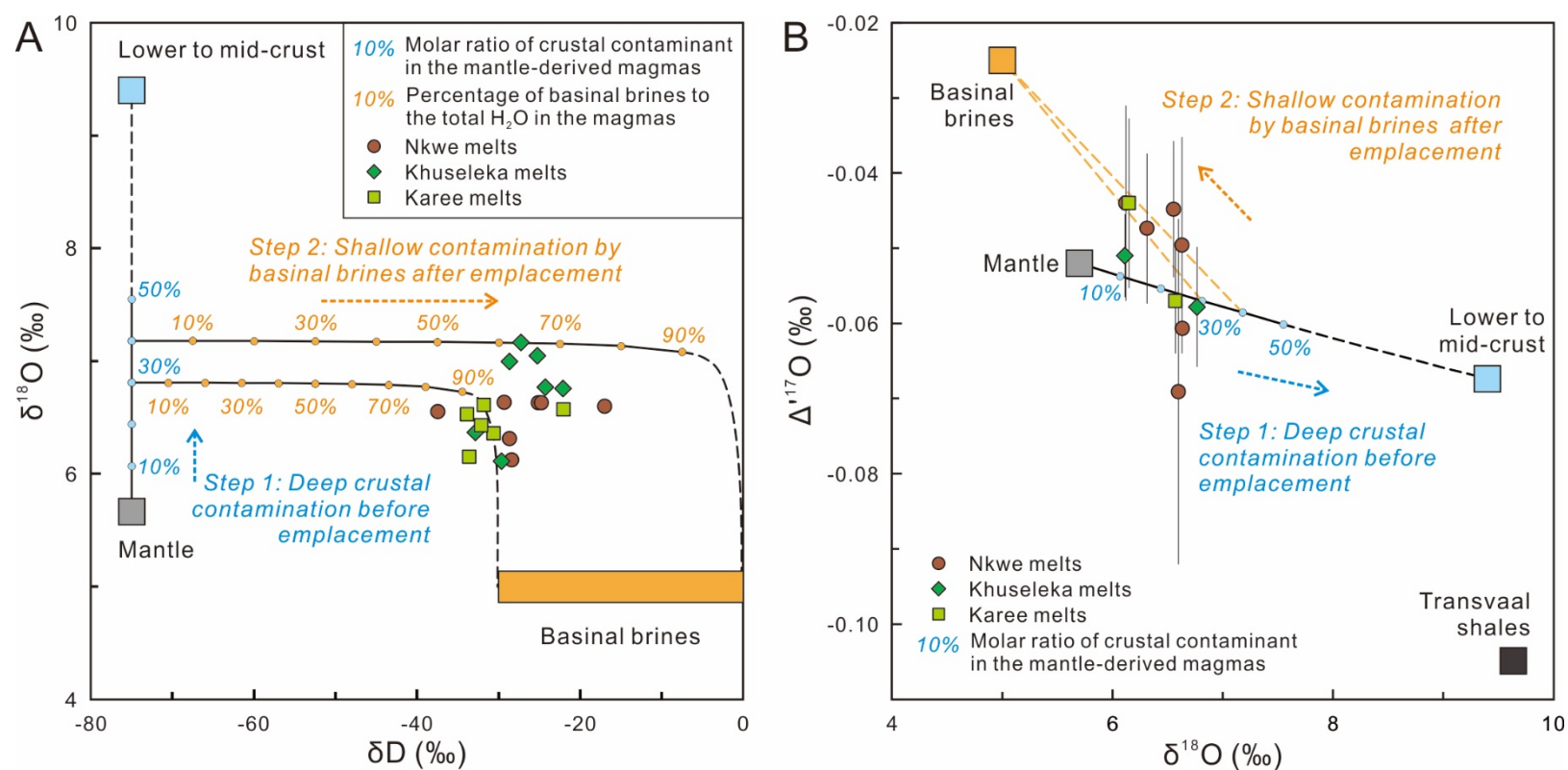
Figure S7. $\delta^{18}O$–δD (A) and $\Delta'^{17}O$–$\delta^{18}O$ (B) plots showing two-step mixing model ($\Delta'^{17}O$ is shown with 1 standard deviation; see the *Methodology* section for data sources and model details). Step 1 (following Harris et al., 2005) is contamination of mantle-derived magmas with Archean rocks (orthogneiss, high-grade metapelites) in lower to middle crust; step 2 is shallow emplacement of contaminated Rustenburg Layered Suite (Bushveld Complex, South Africa) magmas into the Transvaal Basin and incorporation of basinal brines (connate seawater) into UG2 melts. The data for shales in the Transvaal Supergroup are from Bindeman et al. (2018).

TABLE S1. Microprobe data of phlogopite from the UG2 chromitite and adjacent silicate cumulates (Bushveld Complex, South Africa) from the Nkwe, Khuseleka, and Karee mines (supplementary spreadsheet).

TABLE S2. H_2O content (wt%), hydrogen and triple-oxygen isotopic ratios (‰) of phlogopite separates from the UG2 chromitite and adjacent silicate cumulates (Bushveld Complex, South Africa) in the Nkwe, Khuseleka, and Karee mines.

Sample No.	Depth (cm)	Rock type	H_2O	δD	$\delta D_m{}^a$	$\delta^{18}O$	$\delta^{17}O$	$\Delta'^{17}O^b$	$\pm\,\Delta'^{17}O$
Nkwe (eastern Bushveld)									
15-I[c]	2.5	pyroxenite	1.46	−43.1	−30.5				
16A-I[c]	12.5	anorthosite	1.55	−28.6	−16.0				
18A-I	37.5	chromitite	3.22	−29.3	−28.4	5.22	2.72	−0.044	0.013
18A-II	42.5	chromitite	2.71	−29.5	−28.7	5.41	2.82	−0.047	0.010
19A-I	48.5	chromitite	3.10	−30.2	−29.3	5.74	2.98	−0.061	
19B-I	55.5	chromitite	3.96	−38.2	−37.5	5.65	2.95	−0.045	0.009
20A-I	63.5	chromitite	3.11	−25.8	−25.1	5.73	2.99	−0.050	0.014
			3.09[d]	−25.5[d]	−24.8				
20B-I[c]	75.5	pyroxenite	2.79	−33.9	−24.8				
23A-I	131.5	pyroxenite	2.53	−26.1	−17.0	5.70	2.95	−0.069	0.023
Khuseleka (western Bushveld)									
11(4)	4.0	pyroxenite	3.15	−26.1	−21.2	5.92			
10(1)	26.5	pyroxenite	2.90	−30.2	−22.0	5.67	2.95	−0.057	0.007
8(2)	35.0	pyroxenite	3.31	−38.7	−30.6	5.46			
7(2)	45.0	chromitite	3.08	−33.0	−31.8	5.71			
6(2)	54.0	chromitite	3.06	−34.6	−33.9	5.63			
5(4)	68.0	chromitite	3.20	−32.4	−32.2	5.53			
5(2)	75.0	chromitite	3.28	−34.3	−33.6	5.25	2.74	−0.044	0.011
4(2)	94.5	chromitite	2.92	−31.3	−30.6	5.47			
3(5)	102.5	chromitite	3.32	−33.5	−32.8	5.42			
Karee (western Bushveld)									
4048-19	77.0	chromitite	3.30	−30.2	−29.7	5.21	2.71	−0.051	0.006
4048-21	90.0	chromitite	2.97	−33.7	−32.9	5.47			
			3.10[d]	−32.2[d]	−31.4				
4049-2	65.0	chromitite	3.45	−28.0	−27.3	6.26			
4049-4	80.0	chromitite	3.45	−25.8	−25.3	6.15			
						6.23[d]			
4049-6II	98.0	chromitite	3.15	−23.4	−22.1	5.87	3.05	−0.058	0.008
			3.17[d]	−25.6[d]	−24.3	5.85[d]			
4049-6I	114.0	chromitite	3.32	−29.7	−28.7	6.10			

[a] Magmatic δD (δD_m) on the basis of the average values of the compositionally-dependent isotope fraction factors $\Delta D_{phlogopite-water}$ showed in Table S1.

[b] $\Delta'^{17}O = \delta'^{17}O - 0.5305 \times \delta'^{18}O$, where $\delta'^{17,18}O = 1000 \times \ln(\delta^{17,18}O/1000 + 1)$.

[c] Separates contain significant amounts of anhydrous minerals, so their H_2O contents are lower and oxygen isotopes were not analyzed.

[d] Duplicate analyses run for hydrogen and/or oxygen isotopes.